

# The dynamics and excitation of torsional waves in geodynamo simulations

R. J. Teed, C. A. Jones and S. M. Tobias

*Dept. of Applied Mathematics, University of Leeds, Leeds, LS2 9JT, UK. Email: R.J.Teed@leeds.ac.uk*

13 June 2021

## SUMMARY

The predominant force balance in rapidly rotating planetary cores is between Coriolis, pressure, buoyancy and Lorentz forces. This magnetostrophic balance leads to a Taylor state where the spatially averaged azimuthal Lorentz force is compelled to vanish on cylinders aligned with the rotation axis. Any deviation from this state leads to a torsional oscillation, signatures of which have been observed in the Earth's secular variation and are thought to influence length of day variations via angular momentum conservation. In order to investigate the dynamics of torsional oscillations, we perform several three-dimensional dynamo simulations in a spherical shell. We find torsional oscillations, identified by their propagation at the correct Alfvén speed, in many of our simulations. We find that the frequency, location and direction of propagation of the waves are influenced by the choice of parameters. Torsional waves are observed within the tangent cylinder and also have the ability to pass through it. Several of our simulations display waves with core travel times of 4 to 6 years. We calculate the driving terms for these waves and find that both the Reynolds force and ageostrophic convection acting through the Lorentz force are important in driving torsional oscillations.

**Key words:** Torsional oscillation – Taylor state – Rapid rotation – Geodynamo

## 1 INTRODUCTION

Rapidly rotating planetary dynamos, including the geodynamo, are believed to be operating under the magnetostrophic regime, (see, for example, Jones, 2011). In this regime, although the Lorentz force may be locally strong, the averaged azimuthal Lorentz force must vanish on geostrophic cylinders (Taylor, 1963). A dynamo with a magnetic field organised in such a way is said to be in a Taylor state, which provides a severe constraint for dynamo generated fields. Any violation of the state can be represented as an acceleration of the cylinders and stretches radial magnetic field into azimuthal field. The resultant Lorentz force acts like a torsional spring in an attempt to restore the Taylor state (Braginsky, 1970) and leads to the driving of torsional oscillations (TOs) of the cylinders. These oscillations, which are dependent only on cylindrical radius and time, are a type of Alfvén wave (Alfvén, 1942).

Torsional waves are believed to be continually driven in the Earth's core and are traceable in observational data. However, there has been some ambiguity as to the period for the fundamental modes of the torsional oscillations. Early observational data (Braginsky, 1984) inferred a decadal timescale; however more recent data obtained from core flow models by Gillet et al. (2010) show a much shorter period of approximately 6 years. Previous work (Jault et al.,

1988; Jackson, 1997; Zatman & Bloxham, 1997; Bloxham et al., 2002; Buffett et al., 2009) has suggested that torsional oscillations may be responsible for various observed features of the Earth's dynamics; these include changes in length-of-day variations (Jault et al., 1988; Jackson, 1997) and geomagnetic jerks (Bloxham et al., 2002). Additionally, it may be possible to infer information about the magnetic field within the core via core flow models (Zatman & Bloxham, 1997; Buffett et al., 2009). This is useful since geomagnetic data from the Earth's surface can only be reliably transferred down as far as the core-mantle boundary (CMB) (Gubbins & Bloxham, 1985).

Numerical simulations are an obvious tool to analyse the dynamics of torsional waves; however, difficulties arise owing to the inability to reach appropriate Earth-like parameter values. Previous efforts (Dumberry & Bloxham, 2003; Busse & Simitev, 2005; Wicht & Christensen, 2010) to locate torsional waves in simulations have been undertaken with Wicht & Christensen (2010) providing the most clear evidence yet of their observation in the region outside the tangent cylinder (OTC). A recent study by Schaeffer et al. (2012) has focused on the reflection of Alfvén waves at boundaries. They suggest that simulations run with rigid boundary conditions cannot exhibit wave reflection when the viscosity is too large.

We investigate torsional wave production and dynamo

ics in numerical simulations. We employ a systematic exploration of available parameter space and include analysis of the region inside the tangent cylinder (ITC) which was omitted in previous studies. This allows us to attempt to observe not only torsional waves ITC but also the propagation of such waves across the tangent cylinder (TC). We estimate core travel times for the oscillations and, by band-pass filtering our data, we are able to determine whether the timescales that identified TOs operate on are correct. We also explore possible excitation mechanisms by calculating the relevant driving terms. In particular, we separate the Lorentz force into its constituent parts: a restoring force and a driving force.

## 2 MATHEMATICAL FORMULATION

We adapt the model described by Jones et al. (2011) to incompressible systems (using the Boussinesq approximation). We shall extend to the compressible parameter space in future work. Our geometry is based on the Earth's core using a spherical polar coordinate system,  $(r, \theta, \phi)$ . We consider a spherical shell that is radially bounded above at  $r = r_o$  by an electrically insulating mantle and below at  $r = r_i$  by an electrically insulating inner core. The system rotates about the vertical ( $z$ -axis) with rotation rate  $\Omega$  and gravity acts radially inward so that  $\mathbf{g} = -g\mathbf{r}$ . The fluid is assumed to have constant values of  $\rho$ ,  $\nu$ ,  $\kappa$  and  $\eta$ , the outer core density, kinematic viscosity, thermal diffusivity and magnetic diffusivity respectively.

Several recent papers (Sakuraba & Roberts, 2009; Hori et al., 2010; Christensen et al., 2010) have argued that allowing for internal heat sources (or sinks) and imposing fixed heat flux (as opposed to fixed temperature) thermal boundary conditions in models may significantly influence the generation of solutions with Earth-like magnetic field morphologies. Therefore, following the approach of Hori et al. (2010), we also introduce a source of internal heating,  $\epsilon$ , to the temperature equation. The internal heating must satisfy the heat flux equation so that

$$\frac{4\pi}{3}\epsilon(r_o^3 - r_i^3) = 4\pi\kappa r_i^2 \left. \frac{\partial T}{\partial r} \right|_{r=r_i} - 4\pi\kappa r_o^2 \left. \frac{\partial T}{\partial r} \right|_{r=r_o}, \quad (1)$$

where  $T$  is the temperature. We nondimensionalize the basic system of equations on the length scale,  $D = r_o - r_i$ , magnetic timescale,  $D^2/\eta$ , temperature scale,  $\epsilon D^2/\eta$ , and magnetic scale,  $\sqrt{\rho\mu_0\Omega\eta}$ . The relevant system of coupled equations for velocity,  $\mathbf{u}$ , magnetic field,  $\mathbf{B}$ , temperature,  $T$ , and pressure,  $p$  are:

$$\frac{\partial \mathbf{u}}{\partial t} + (\mathbf{u} \cdot \nabla)\mathbf{u} = -\frac{Pm}{E} [\nabla p + 2\hat{\mathbf{z}} \times \mathbf{u} - (\nabla \times \mathbf{B}) \times \mathbf{B}] + \frac{Pm^2 Ra}{Pr} \mathbf{T}\mathbf{r} + Pm \nabla^2 \mathbf{u}, \quad (2)$$

$$\frac{\partial T}{\partial t} + (\mathbf{u} \cdot \nabla)T = \frac{Pm}{Pr} \nabla^2 T + \text{sgn}(\epsilon), \quad (3)$$

$$\frac{\partial \mathbf{B}}{\partial t} - \nabla \times (\mathbf{u} \times \mathbf{B}) = \nabla^2 \mathbf{B}, \quad (4)$$

$$\nabla \cdot \mathbf{u} = 0, \quad (5)$$

$$\nabla \cdot \mathbf{B} = 0. \quad (6)$$

Equations (2) to (4) are the incompressible Navier-Stokes, temperature and induction equations respectively and (5) and (6) describe the solenoidal conditions for velocity and magnetic field. The nondimensional parameters appearing in our equations are the Rayleigh number,  $Ra$ , Ekman number,  $E$ , Prandtl number,  $Pr$ , and magnetic Prandtl number,  $Pm$ , defined by:

$$Ra = \frac{g\alpha|\epsilon|D^5}{\nu\kappa\eta}, \quad E = \frac{\nu}{\Omega D^2}, \quad Pr = \frac{\nu}{\kappa}, \quad Pm = \frac{\nu}{\eta}. \quad (7)$$

The radius ratio,  $\beta = r_i/r_o$ , is an additional parameter but in this work we restrict ourselves to the value appropriate to the Earth's core, namely  $\beta = 0.35$ . Note that under the nondimensionalization chosen, the internal heating term has been scaled to unity. However, in order to maintain a consistent physical problem, via (1), the internal heating may be either a source or a sink resulting in the need for the  $\text{sgn}(\epsilon)$  function in (3). The magnitude of  $\epsilon$  appears only in the definition of the Rayleigh number. In this definition of  $Ra$  the quantity  $|\epsilon|$  occupies the driving role usually taken by the temperature difference across the domain which appears in the classical definition of the Rayleigh number.

## 3 THEORY AND METHODS

### 3.1 Taylor's constraint and torsional oscillations

The analysis of torsional oscillations requires consideration of the forces on geostrophic cylinders and hence the introduction of a cylindrical polar coordinate system,  $(s, \phi, z)$ , is beneficial. Averages over  $\phi$  and  $z$  are required and hence for any scalar field  $A$  we define

$$\bar{A}(t, s, z) = \frac{1}{2\pi} \int_0^{2\pi} A d\phi, \quad \langle A \rangle(t, s, \phi) = \frac{1}{h} \int_{z_-}^{z_+} A dz. \quad (8)$$

Here  $h(s) = z_+(s) - z_-(s)$  and OTC we simply have that  $z_{\pm} = \pm\sqrt{r_o^2 - s^2}$ . Within the tangent cylinder the definition of  $z_{\pm}$  may remain the same if an average over the entire  $z$  domain is desired. However, ITC we may wish to average over the two hemispheres separately, which we refer to as ITCN and ITCS for north and south of the inner core respectively. For ITCN (ITCS) we then have that  $z_+ = \sqrt{r_o^2 - s^2}$  and  $z_- = \sqrt{r_i^2 - s^2}$  ( $z_+ = -\sqrt{r_i^2 - s^2}$  and  $z_- = -\sqrt{r_o^2 - s^2}$ ).

For later convenience, we also define two further quantities for a scalar, or vector, field  $A$ . The first of these quantities,  $\bar{A}$ , is simply the time average of  $A$  over some time period,  $\tau$ . The second quantity,  $A'$ , is the fluctuating part of  $A$ . Therefore we define  $\bar{A}$  and  $A'$  by

$$\bar{A}(s, \phi, z) = \frac{1}{\tau} \int_0^{\tau} A dt \quad \text{and} \quad A'(t, s, \phi, z) = A - \bar{A}, \quad (9)$$

respectively.  $A'$  is useful because it removes from  $A$  the mean background state which only varies on a long timescale. Standard torsional oscillation theory relies on the ability to separate the timescales in this way successfully.

The  $\phi$  and  $z$  averages of the  $\phi$ -component of (2) illustrate the forces that can accelerate geostrophic cylinders. Three such forces can be identified (Wicht & Christensen, 2010); namely the Reynolds force, Lorentz force and viscous

142 force leading to the equation

$$\begin{aligned} \frac{\partial \langle \overline{u_\phi} \rangle}{\partial t} &= -\langle \hat{\phi} \cdot (\nabla \cdot \mathbf{u}\mathbf{u}) \rangle + PmE^{-1} \langle \hat{\phi} \cdot ((\nabla \times \mathbf{B}) \times \mathbf{B}) \rangle \\ &\quad + Pm \langle \hat{\phi} \cdot \nabla^2 \mathbf{u} \rangle \\ &\equiv F_R + F_L + F_V. \end{aligned} \quad (10)$$

143 The Coriolis and buoyancy forces have vanished during the  
144 integration process since in the former there is no net flow  
145 across the cylinder and no  $\phi$ -component in the latter. This  
146 has consequences in the core where the fluid is believed, at  
147 leading order, to be in magnetostrophic balance (between  
148 Lorentz, Coriolis and Archimedean forces). Taylor (1963)  
149 noted that in systems where the force balance is magne-  
150 tostrophic the constraint

$$F_L = 0, \quad (11)$$

151 arises.

152 The Lorentz force can be partially integrated (see, for  
153 example, Wicht & Christensen (2010)) to give

$$F_L = \frac{Pm}{E} \frac{1}{hs^2} \frac{\partial}{\partial s} s^2 h \langle \overline{B_s B_\phi} \rangle + \frac{Pm}{E} \frac{1}{h} \left[ \frac{s}{z} \overline{B_s B_\phi} + \overline{B_z B_\phi} \right]_{z_-}^{z_+}. \quad (12)$$

154 We are able to neglect the magnetic coupling terms in this  
155 expression at this stage due to our use of insulating bound-  
156 ary conditions at both the CMB and the inner core bound-  
157 ary (ICB) (Jones et al., 2011). However, if one were to allow  
158 for a conducting inner core (or mantle), the contribution  
159 from these surface terms would be nonzero resulting in an  
160 additional forcing in the system that is not discussed fur-  
161 ther here. For discussion of how this coupling term arises  
162 see Roberts & Aurnou (2012).

163 Upon consideration of the time derivative of the expres-  
164 sion for  $F_L$  in (12) we find that we require expressions for  
165 the time derivatives of components of the magnetic field. We  
166 substitute from the induction equation and retain *all terms*  
167 on the right-hand-side of (4), to determine that

$$\begin{aligned} \dot{F}_L &= \frac{Pm}{E} \frac{1}{hs^2} \frac{\partial}{\partial s} s^2 h \langle \overline{\dot{B}_s B_\phi + B_s \dot{B}_\phi} \rangle \\ &= \frac{Pm}{E} \frac{1}{hs^2} \frac{\partial}{\partial s} s^2 h \left\{ \left\langle \overline{s B_s (\mathbf{B} \cdot \nabla) \frac{u_\phi}{s}} \right\rangle \right. \\ &\quad \left. + \left\langle \overline{\frac{B_\phi}{s} (\mathbf{B} \cdot \nabla) (s u_s)} \right\rangle \right. \\ &\quad \left. - \left\langle \overline{\left( \mathbf{u} \cdot \nabla + \frac{2}{s^2} \right) (B_s B_\phi)} \right\rangle \right. \\ &\quad \left. + \langle \overline{B_s \nabla^2 B_\phi + B_\phi \nabla^2 B_s} \rangle \right\}. \end{aligned} \quad (13)$$

163 In order to make further progress we use the definitions of (9)  
164 to split the velocity and magnetic field into mean and fluctu-  
165 ating parts. Previous studies (Wicht & Christensen, 2010;  
166 Roberts & Aurnou, 2012) have essentially assumed that the  
167 mean quantities,  $\tilde{\mathbf{u}}$  and  $\tilde{\mathbf{B}}$ , are the principal parts of the  
168 Taylor state and that the fluctuating quantities,  $\mathbf{u}'$  and  $\mathbf{B}'$ ,  
169 are perturbations associated with the TOs. However, this is  
170 not the full picture since it requires the assumption that  $\mathbf{u}'$   
171 is purely geostrophic as explicitly stated by Taylor (1963).  
172 In reality the convection will be operating, to some degree,  
173 on all timescales and this phenomenon is likely to be an im-  
174 portant driving mechanism. Hence rather than assuming a  
175 geostrophic form for our velocity fluctuation we instead split

176 it into geostrophic ( $s\zeta'$ ) and ageostrophic parts ( $\mathbf{u}'_A$ ) so that

$$\mathbf{u} = \tilde{\mathbf{u}} + \mathbf{u}' = \tilde{\mathbf{u}} + s\zeta'(s, t)\hat{\phi} + \mathbf{u}'_A, \quad \mathbf{B} = \tilde{\mathbf{B}} + \mathbf{B}'. \quad (15)$$

177 Upon substitution of these forms into our expression for  $\dot{F}_L$ ,  
178 we find that  $\zeta'$  only appears in the first term on the right-  
179 hand-side of (14). Considering only the mean magnetic field  
180 parts of this term and calling it  $\dot{F}_{LR}$  gives

$$\dot{F}_{LR} = \frac{1}{hs^2} \frac{\partial}{\partial s} \left( s^3 h U_A^2 \frac{\partial \zeta}{\partial s} \right), \quad U_A = \sqrt{\frac{Pm}{E} \langle \overline{B_s^2} \rangle}, \quad (16)$$

181 where we have defined the Alfvén speed,  $U_A$ . Equation (14)  
182 can then be written as

$$\dot{F}_L = \dot{F}_{LR} + \dot{F}_{LD}, \quad (17)$$

183 where  $\dot{F}_{LD}$  is a complicated expression made up of the re-  
184 maining terms on the right-hand-side of (14). Thus it in-  
185 volves terms containing the components of  $\tilde{\mathbf{B}}$ ,  $\mathbf{B}'$ ,  $\tilde{\mathbf{u}}$ ,  $\mathbf{u}'_A$ , as  
186 well as  $\zeta'$ .

187 If we now take the time derivative of (10) and use the  
188 result of (17) we find that

$$s\dot{\zeta}' = \dot{F}_{LR} + \dot{F}_{LD} + \dot{F}_R + \dot{F}_V, \quad (18)$$

189 noting that  $\langle \overline{\hat{\phi} \cdot \mathbf{u}'_A} \rangle = 0$  by definition. By writing the ex-  
190 pression for  $\dot{\zeta}'$  in this way we have been able to separate  
191 the term involved in the balance of the torsional wave equa-  
192 tion from the remaining terms. The standard canonical wave  
193 equation as found in previous work (see, for example, Bra-  
194 ginsky, 1970) is represented by  $s\dot{\zeta}' = \dot{F}_{LR}$ . Consequently, if  
195 we time integrate (18) to acquire

$$s\dot{\zeta}' - F_{LR} = F_{LD} + F_R + F_V, \quad (19)$$

196 we find that  $F_{LR}$  is the restoring force whereas  $F_{LD}$ ,  $F_R$  and  
197  $F_V$  are driving forces.

198 Torsional waves in the core must be driven and dissipa-  
199 ted by some mechanism(s) and hence the terms on the  
200 right-hand-side of (19), namely  $F_R$ ,  $F_V$  and  $F_{LD}$ , fulfil this  
201 role. They are driving (and dissipative) forces which are able  
202 to create, destroy and alter the nature of propagating tor-  
203 sional waves. When performing diagnostics on our simula-  
204 tions, one of our interests will be analysing the terms on the  
205 right-hand-side of (19). This will allow us to identify which  
206 forces are able to act as excitation mechanisms at various  
207 points in the domain. We look at this in section 4.5.

### 208 3.2 Output parameters

In addition to quantities described in subsection 3.1 we also  
output several other parameters from our simulations. The  
magnetic Reynolds number, Elsasser number, Rossby num-  
ber and dipole moment are defined by

$$Rm = \frac{UD}{\eta}, \quad (20)$$

$$\Lambda = \frac{|B|^2}{\rho\mu\eta\Omega}, \quad (21)$$

$$Ro = \frac{U}{\Omega D}, \quad (22)$$

$$f_{\text{dip}} = \left( \frac{E_M^{(1,0)}(r_o)}{\sum_{l=1}^{12} \sum_{m=0}^l E_M^{(l,m)}(r_o)} \right)^{1/2}, \quad (23)$$

209 respectively. Here  $E_M^{(l,m)}(r)$  represents the magnetic energy  
 210 in the  $(l, m)$  harmonic at radius  $r$ . Owing to our choice of  
 211 nondimensionalization, the magnetic Reynolds and Elsasser  
 212 numbers can be identified with the nondimensional velocity  
 213 and square of the magnetic field respectively. The param-  
 214 eters defined in equations (20) to (23) give an indication of  
 215 the sort regime that the dynamo is in, a point we address in  
 216 section 4.1.

### 217 3.3 Methods

218 We perform several simulations, using the Leeds spherical  
 219 dynamo code (Jones et al., 2011) which uses a pseudo-  
 220 spectral numerical scheme with finite differences in the ra-  
 221 dial direction. We run the code at parameter regimes and  
 222 with boundary conditions that facilitate the production of  
 223 Earth-like dynamos. Guided by previous work (Hori et al.,  
 224 2010) we therefore employ the use of fixed flux thermal  
 225 boundary conditions for all of our simulations. Specifically,  
 226 we set zero flux on the CMB and the flux entering at the  
 227 ICB is then balanced by a sink term in the temperature  
 228 equation; that is,  $\text{sgn}(\epsilon) = -1$ . This mathematical setup is,  
 229 in a physical sense, representative of a model for composi-  
 230 tional convection. Rigid kinematic boundary conditions are  
 231 primarily used, although one set of simulations is repeated  
 232 with stress-free boundaries as way of comparison.

233 In parameter space we perform simulations at a range of  
 234 Ekman numbers since the existence of torsional oscillations  
 235 requires the dynamo to be near magnetostrophic balance,  
 236 which in turn is dependent on a small Ekman number. Thus,  
 237 by decreasing the Ekman number over the range  $10^{-4}$  to 269  
 238  $10^{-6}$  torsional oscillations should become more apparent. 270  
 239 We focus on  $Pr = 1$  and each simulation is at the same value  
 240 of criticality; that is  $Ra/Ra_c \simeq 8.32$  for all runs. However,  
 241 we do vary the magnetic Prandtl number,  $Pm \in [1, 5]$ , in  
 242 order to allow for a range in the magnetic field strength. 271  
 243 The values of  $Ra_c$  used are for the onset of non-magnetic 272  
 244 convection (see, for example, Dormy et al., 2004). Table 1  
 245 displays the input parameters for the set of runs performed  
 246 as well as the kinetic boundary conditions employed. 274

247 Each run is initially time integrated from a random 275  
 248 state for at least one tenth of a magnetic diffusion time apart 276  
 249 from run 6R1 which is run for a shorter period due to resolu- 277  
 250 tion constraints. In order to search for torsional oscillations 278  
 251 we then analyse a period of time,  $\tau$ , of every run. The value 279  
 252 of  $\tau$  for each run, indicated in Table 1, is run dependent and 280  
 253 varies between 0.002 and 0.02 of a diffusion time. 281

254 By including the region ITC in our analysis we present 282  
 255 ourselves with a complication since it is not obvious how 283  
 256 to deal with the regions north and south of the inner core. 284  
 257 For example, when performing averages over  $z$  do we average 285  
 258 over the entire vertical from pole to pole or instead retain the 286  
 259 distinction between the hemispheres? Consequently, there is 287  
 260 also the issue of how to treat waves propagating across the 288  
 261 tangent cylinder since they may originate (or terminate) in 289  
 262 either hemisphere. These issues were not present in the pre- 290  
 263 vious work on torsional wave analysis in dynamo simulations 291  
 264 (Wicht & Christensen, 2010) where the region ITC was omit- 292  
 265 ted. We choose to allow for both scenarios by performing 293  
 266 both sets of averages. Therefore in our analysis we average 294  
 267 over the entire region ITC, but also perform averages over 295  
 268 each hemisphere separately (that is over ITCN and ITCS). 296

Run	$E$	$Ra$	$Pr$	$Pm$	BCs	$\tau$
4R1	$10^{-4}$	$4.937 \times 10^6$	1	1	NS	0.02
4R2	$10^{-4}$	$4.937 \times 10^6$	1	2	NS	0.02
4R3	$10^{-4}$	$4.937 \times 10^6$	1	3	NS	0.02
4R4	$10^{-4}$	$4.937 \times 10^6$	1	4	NS	0.014
4R5	$10^{-4}$	$4.937 \times 10^6$	1	5	NS	0.014
5R1	$10^{-5}$	$1 \times 10^8$	1	1	NS	0.006
5R2	$10^{-5}$	$1 \times 10^8$	1	2	NS	0.006
5R3	$10^{-5}$	$1 \times 10^8$	1	3	NS	0.006
5R4	$10^{-5}$	$1 \times 10^8$	1	4	NS	0.003
5R5	$10^{-5}$	$1 \times 10^8$	1	5	NS	0.003
6.5R1	$5 \times 10^{-6}$	$2.493 \times 10^8$	1	1	NS	0.004
6.5R2	$5 \times 10^{-6}$	$2.493 \times 10^8$	1	2	NS	0.004
6.5R3	$5 \times 10^{-6}$	$2.493 \times 10^8$	1	3	NS	0.004
6.5R4	$5 \times 10^{-6}$	$2.493 \times 10^8$	1	4	NS	0.002
6.5R5	$5 \times 10^{-6}$	$2.493 \times 10^8$	1	5	NS	0.002
6R1	$10^{-6}$	$2.132 \times 10^9$	1	1	NS	0.002
5F1	$10^{-5}$	$1.265 \times 10^8$	1	1	SF	0.008
5F2	$10^{-5}$	$1.265 \times 10^8$	1	2	SF	0.005
5F3	$10^{-5}$	$1.265 \times 10^8$	1	3	SF	0.003
5F4	$10^{-5}$	$1.265 \times 10^8$	1	4	SF	0.003
5F5	$10^{-5}$	$1.265 \times 10^8$	1	5	SF	0.002

**Table 1.** Table displaying the parameter sets used for the various simulations. Note that all runs have fixed flux thermal boundary conditions with zero flux on the outer boundary and an internal heat sink.

For the region OTC, averages are always performed across all  $z$ -space.

## 271 4 NUMERICAL RESULTS

### 272 4.1 Field strength and morphology

273 The output parameters calculated from our numerical re-  
 274 sults are displayed in Table 2. In this table we also indi-  
 275 cate, for each run, whether torsional oscillations were iden-  
 276 tified and if so, also the region(s) of the shell that they  
 277 were observed. Within our full set of simulations we are  
 278 able to identify two major magnetohydrodynamic regimes  
 279 for which the fluid in each run can organise itself. The weak  
 280 field regime has  $\Lambda \sim O(1)$  whereas the strong field regime  
 281 has a much larger Elsasser number. As one would expect,  
 282 the latter regime is found at larger values of the magnetic  
 283 Prandtl number. Velocity structures are larger in the strong  
 284 field regime. However, it should be noted that even in the  
 285 weak field regime the convection is not as small scale as one  
 286 may expect for such a rapidly rotating system. This is due  
 287 to the employment of fixed flux thermal boundary condi-  
 288 tions, which have been found to significantly affect the size  
 289 of velocity structures (Hori et al., 2010).

With current estimates that  $Rm \approx 1000$  for the Earth's  
 290 outer core, Table 2 indicates that only our high  $Pm$ , low  $E$   
 291 runs begin to approach Earth-like magnetic Reynolds num-  
 292 bers. However, simulations in the strong field regime produce  
 293 Elsasser numbers too large for the Earth where  $\Lambda \sim O(1)$ .  
 294 The converse is true of the dipolarity, which decreases to  
 295 near Earth-like values for our larger  $Pm$  runs.

Run	$Rm$	$\Lambda$	$Ro$	$f_{\text{dip}}$	$U_A(s=r_o)$	TOs
4R1	98.118	0.896	0.010	0.890	0.067	-
4R2	135.595	1.888	0.007	0.867	1.436	-
4R3	152.387	5.672	0.005	0.847	15.673	-
4R4	183.966	10.358	0.005	0.776	22.262	OTC
4R5	217.046	15.621	0.004	0.741	29.382	OTC,ITC
5R1	128.542	0.319	0.001	0.924	5.015	OTC
5R2	203.348	1.740	0.001	0.904	14.283	OTC,ITC
5R3	330.519	16.197	0.001	0.722	90.073	OTC,ITC
5R4	355.911	17.433	0.001	0.713	90.267	OTC,ITC
5R5	437.071	19.252	0.001	0.742	123.902	OTC
6.5R1	155.4277	0.325	0.001	0.917	7.774	OTC,ITC
6.5R2	267.719	2.400	0.001	0.955	22.078	OTC,ITC
6.5R3	383.569	3.631	0.001	0.946	29.173	OTC,ITC
6.5R4	575.840	23.637	0.001	0.752	259.222	OTC
6.5R5	598.998	20.080	0.001	0.752	243.473	OTC,ITC
6R1	372.872	0.561	< 0.001	0.918	15.664	OTC,ITC
5F1	172.707	0.368	0.002	0.918	5.094	OTC
5F2	226.404	2.164	0.001	0.955	16.588	OTC,ITC
5F3	336.970	18.817	0.001	0.676	94.567	OTC,ITC
5F4	402.806	18.578	0.001	0.738	89.943	OTC,ITC
5F5	560.841	23.636	0.001	0.719	109.473	OTC,ITC

**Table 2.** Table displaying the output parameters calculated for the various simulations.

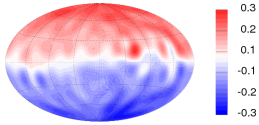


**Figure 1.** The radial magnetic field at the CMB for the run 5R2.

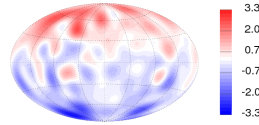


**Figure 2.** The radial magnetic field at the CMB for the run 6.5R5.

In Figs 1 and 2 we plot  $B_r$ , truncated at harmonic degree 12, at the CMB for runs at two different values of  $Pm$ . Although both figures show dipolar fields, the dipolarity is visibly stronger in Fig. 1 than Fig. 2, which has patches of reversed flux. These plots are representative of the radial magnetic field for the two different regimes seen across all of our runs. As we shall discuss later, the two regimes will also have implications on where and what sort of torsional oscillations can be found.

## 4.2 Identification of torsional oscillations

In a similar vein to Wicht & Christensen (2010) we identify torsional oscillations by structures in the azimuthal fields moving radially in  $s$  with the local Alfvén speed. In order to observe features operating on short timescales we analyse the fields with the time average removed; that is we consider  $u'_\phi$  and its spatial average relevant to the problem in hand. For each run we evaluate the quantity  $\langle \tilde{B}_s^2 \rangle$  for use in the definition of  $U_A$ .

Figs 3 and 4 show  $U_A$  as a function of  $s$  for the two runs 6.5R2 and 6.5R5 respectively. Blue and red curves indicate a  $z$ -average over the northern and southern hemisphere respectively whereas the black curve is an average performed

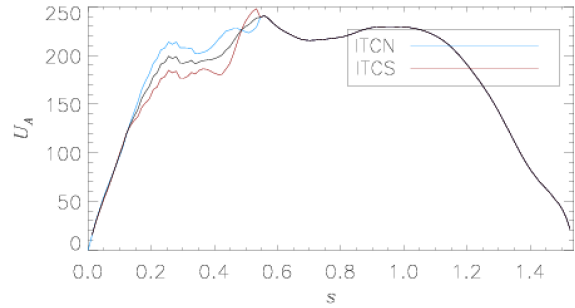


**Figure 3.** Alfvén speed, as a function of  $s$ , for the run 6.5R2.

over all  $z$ -space. These plots are typical for all runs with the same values of  $Pm$  so we do not present further plots of  $U_A$  here. The form of  $U_A$  is broadly similar in the two cases: increasing rapidly from the origin (but not identically zero at  $s = 0$ ), reaching a peak at the TC (clearly located at  $s \approx 0.538$ ) and generally decreasing OTC as the equatorial region at the CMB is approached. The main difference is an increase in the magnitude of the Alfvén speed as the magnetic Prandtl number is increased. This is to be expected owing to the dependence of  $U_A$  on  $Pm$  shown in (16). The only major difference in the form of  $U_A$  at different magnetic Prandtl numbers is that runs with lower  $Pm$  tend to retain their peak Alfvén speed for a significant region OTC. Conversely, at higher  $Pm$  the Alfvén speed, as a function of  $s$ , decreases more or less immediately and monotonically from the TC to the CMB at the equator.

In Figs 5 to 9 we display colour-coded density plots of  $\langle \tilde{u}_\phi \rangle'$  in  $ts$ -space for several runs. For these figures we have chosen runs from both regimes described in section 4.1. Each

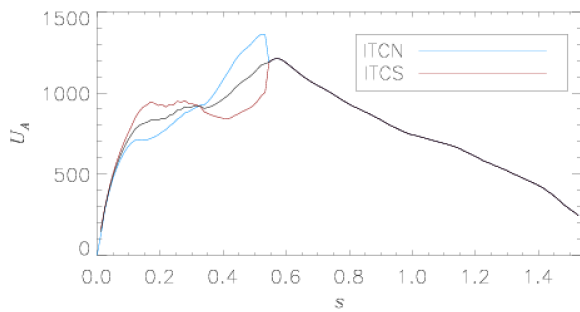


**Figure 4.** Alfvén speed, as a function of  $s$ , for the run 6.5R5.

338 of the figures contains three plots which display the different  
 339 possible averaging domains ITC. The top/middle plot is for  
 340 ITCN/ITCS whereas the bottom plot takes the average over  
 341 the entire  $z$ -domain. Each plot contains the same data OTC.  
 342 Overlaying each plot are several white curves that display  
 343 trajectories that features take when travelling at the Alfvén  
 344 speed,  $U_A$ . Note that these curves do not have a constant  
 345 gradient since the Alfvén speed is a function of  $s$ .

346 The first run that we display plots for is a run with  
 347  $Pm = 5$  and  $E = 10^{-4}$ , which is the largest value of the  
 348 Ekman number considered. Runs in the weak field regime  
 349 were not found to permit TOs at this large an Ekman num-  
 350 ber. In Fig. 5, for run 4R5, several structures in  $\langle \overline{u_\phi} \rangle'$   
 351 can be identified as torsional waves since they follow a trajec-  
 352 tory predicted by  $U_A$ . These features appear regularly and  
 353 can be seen to originate at various locations of the domain  
 354 indicating that the waves can, but are not obliged to appear  
 355 from the TC. Within the tangent cylinder a wave propa-  
 356 gates inwards from the TC in the northern hemisphere (at  
 357  $t \simeq 0.011$ ); the only feature to do so in this run.

358 In Figs 6 (for a weak field regime at  $Pr = 2$ ) and 7 (for  
 359 a strong field regime at  $Pr = 5$ ) the Ekman number has  
 360 been reduced by an order of magnitude compared with Fig.  
 361 5. In both sets of plots several torsional oscillations are again  
 362 immediately apparent. Features in  $\langle \overline{u_\phi} \rangle'$  travel slower in the  
 363 lower  $Pm$  case owing to the smaller magnetic field strength  
 364 generated at lower magnetic Prandtl number. However, it is  
 365 certainly noticeable, from the timescale on the plots alone,  
 366 that waves are propagating significantly faster at lower Ek-  
 367 man number, as expected from (16).

368 There is evidence of an inward propagating wave pass-  
 369 ing through the tangent cylinder (at  $s \approx 0.538$ ) in Fig. 6  
 370 shortly after  $t = 0.002$ . It is clear from the top and middle  
 371 plots that this wave continues to propagate in the southern  
 372 hemisphere ITC but does not ITCN. At  $t \simeq 0.005$  a second  
 373 structure again appears to pass through the TC, this time  
 374 in both hemispheres. Run 5R2 also has an approximately  
 375 similar number of inward and outward propagating waves.  
 376 Conversely, run 5R5 is dominated by two structures origi-  
 377 nating at the TC and moving radially outwards towards the  
 378 equator at the CMB. Neither inwards propagating TOs nor  
 379 TOs within the TC were identified in this run.

380 When the Ekman number is reduced further to  $E =$   
 381  $5 \times 10^{-6}$ , for runs 6.5R2 and 6.5R5, we continue to observe  
 382 faster moving waves with lower Ekman number. Other than  
 383 the difference in the speed of the waves, run 6.5R2 is rather

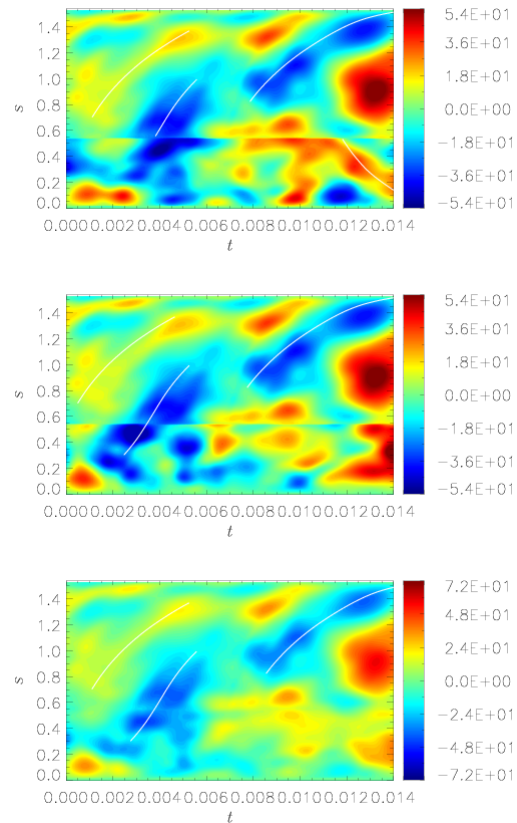


**Figure 5.** Azimuthal velocity,  $\langle \overline{u_\phi} \rangle'$ , for the run 4R5, as a function of distance,  $s$ , from the rotation axis and time,  $t$ , in magnetic diffusion units.

384 similar to run 5R2 since Fig. 8 displays several oscillations  
 385 propagating both inwards and outwards as well as persis-  
 386 tence through the TC. There are TOs propagating from the  
 387 TC in run 6.5R5 as well as possible evidence of waves ITC  
 388 propagating in either direction. However, several of the fea-  
 389 tures highlighted with white curves in Fig. 9 will become  
 390 more apparent when we apply bandpass filtering and thus  
 391 we retain further discussion until section 4.4.

392 Figs 10 and 11 show a series of snapshots of  $\overline{u_\phi}'$  in  
 393 a meridional section for two runs. In the first set of snap-  
 394 shots, for run 5R2, we see that the azimuthal velocity is very  
 395 columnar both inside and outside the TC. However, it proves  
 396 difficult to see evidence of propagation of these columns ei-  
 397 ther inwards or outwards. Analysis of a movie shows occa-  
 398 sional propagation of columns but for the most part the  
 399 oscillations act as standing waves. This is to be expected  
 400 because we observed from Fig. 6 that this run contains both  
 401 inwards and outwards moving waves in approximately equal  
 402 numbers. Therefore it is tricky to distinguish between the  
 403 two directions of travel.

404 Although the columnar structure of Fig. 11, for run 4R5,  
 405 is less striking, we are able to observe features moving radi-  
 406 ally outwards. Between  $t = 0.009$  and  $t = 0.010$  a positive  
 407 (red) structure in  $\overline{u_\phi}'$  propagates towards the equator and by  
 408  $t = 0.012$  it has dissipated at the boundary. This is shortly  
 409 followed by a negative (blue) structure that at  $t = 0.009$   
 410 resides in the centre of the region OTC but by  $t = 0.014$  has  
 411 moved to the equator as a newly formed positive structure



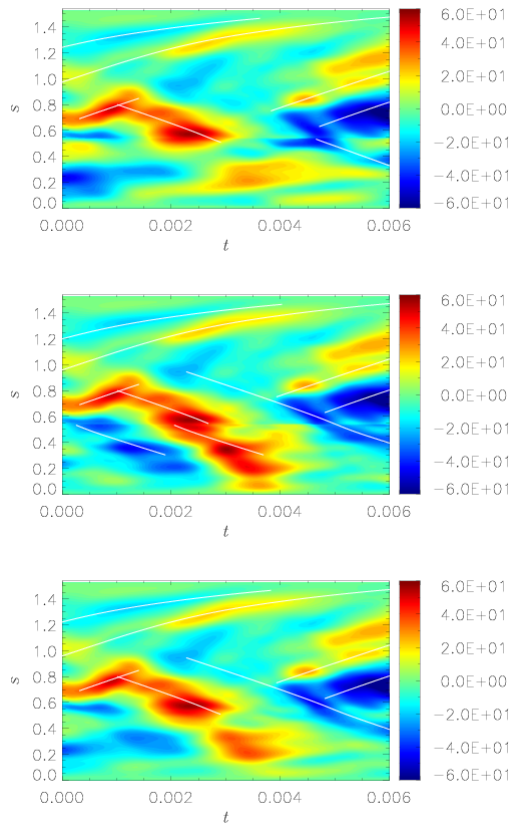


Figure 6. Azimuthal velocity,  $\langle \overline{u_\phi} \rangle'$ , for the run 5R2.

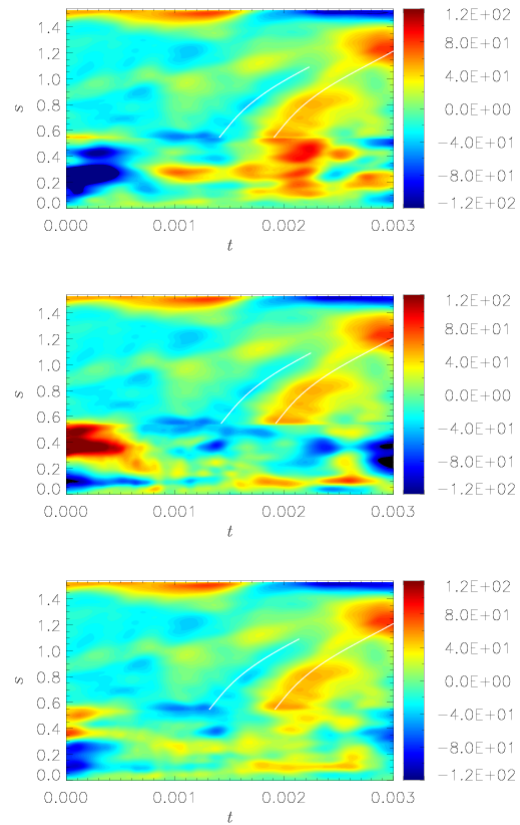


Figure 7. Azimuthal velocity,  $\langle \overline{u_\phi} \rangle'$ , for the run 5R5.

412 now dominates OTC. These outwards propagating positive  
413 and negative features can be directly matched with those of  
414 Fig. 5 for the section of time from  $t = 0.009$  to  $t = 0.014$ .

415 The plots displayed, and more generally the runs con-  
416 sidered, in this subsection are representative of other runs  
417 from Table 1 that are in neighbouring regions of parameter  
418 space. The general features observed in the figures can be  
419 extrapolated to the runs for which we have not displayed  
420 plots. For example, runs with  $Pm = 1$  are found to have  
421 an even more columnar structure with even fewer propagat-  
422 ing waves compared with the  $Pm = 2$  cases. Additionally,  
423 we find that repeating runs with stress-free boundary  
424 conditions do not appear to alter our findings from the rigid  
425 case since various plots of the data for the runs 5F1 to 5F5  
426 broadly match those of runs 5R1 to 5R5. This is, perhaps,  
427 not surprising when reflecting on the similarity of the output  
428 parameters from these two sets of runs (Table 2).

429 One feature of TOs that we have not observed is the  
430 possible reflection of waves at the equator. This is true not  
431 only for the runs for which we have displayed plots, but,  
432 more generally, is the case across all of our simulations. Our  
433 results are therefore in agreement with Schaeffer et al. (2012)  
434 who suggest that the observation of wave reflection in dy-  
435 namo simulations with insulating no-slip BCs is not possible  
436 due to a small reflection coefficient.

### 437 4.3 Core travel times

438 We are able to estimate the travel time for our observed  
439 waves to cross the outer core. However, such estimates must  
440 be treated with a considerable degree of caution since the  
441 parameter regimes used to produce these simulations are  
442 inconsistent with that of the Earth resulting in a difficulty  
443 in identifying the timescale to use when converting back  
444 from our nondimensional time to physical time.

445 Consideration of the diffusion timescale reveals that it is  
446 not ideal for conversion in our study of TOs since our fields in  
447 these units are often too strong. Therefore we choose to con-  
448 vert by matching the Alfvén speed at the CMB. Using  $0.7\text{mT}$   
449 as the magnetic field strength at the CMB (Gillet et al.,  
450 2010) and  $\rho = 1 \times 10^4 \text{kgm}^{-3}$  (as well as  $\mu_0 = 4\pi \times 10^{-7}$ )  
451 this gives an Alfvén speed of approximately  $6 \times 10^{-3} \text{ms}^{-1}$   
452 at the CMB.

453 We can use the values of  $U_A(r_o)$  (the Alfvén speed at  
454 the equator at the CMB) given in Table 2, as well as  $D \approx$   
455  $2.2 \times 10^6 \text{km}$ , to calculate the dimensional version of  $\tau$  from  
456 Table 1. Since TOs are approximately operating on the  $\tau$   
457 timescale we thus find that the outer core travel time of the  
458 TOs in our simulations ranges from months to  $\approx 6$  years.  
459 TOs in the core are currently believed (Gillet et al., 2010)  
460 to operate on a 4 to 6 year timescale and, from our set of  
461 simulations, it is runs in the strong field regime that fare  
462 best at operating on or near to this timescale. In particular,  
463 runs 4R5, 5R3, 5R4, 5R5, 6.5R4 and 6.5R5 have all shown  
464 TOs with core crossing travel times in the 4 to 6 year range.

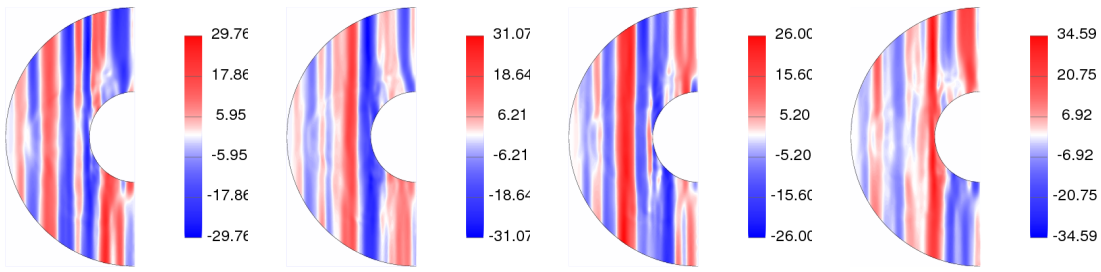


**Figure 10.** Series of snapshots of  $\overline{u_\phi}'$  for the run 5R2. Panels from left to right are at the following times:  $t = 0.0004$ ,  $t = 0.0008$ ,  $t = 0.0012$ , and  $t = 0.0016$ .

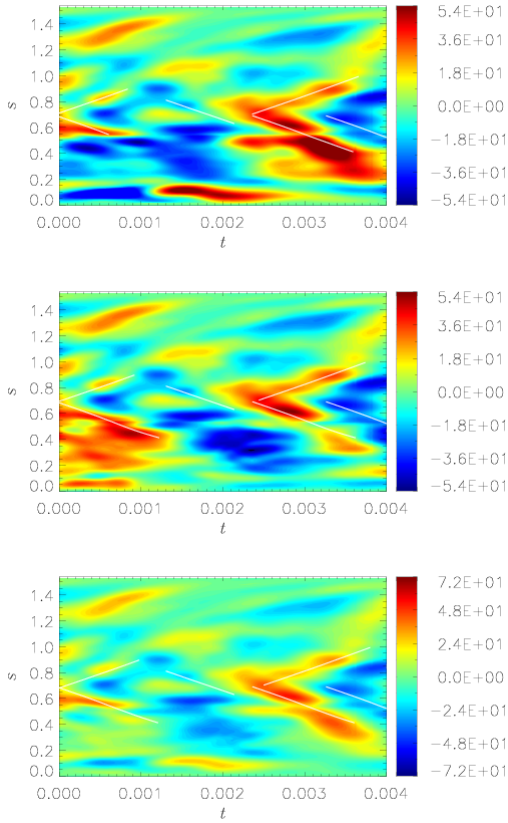


**Figure 8.** Azimuthal velocity,  $\langle \overline{u_\phi} \rangle'$ , for the run 6.5R2.

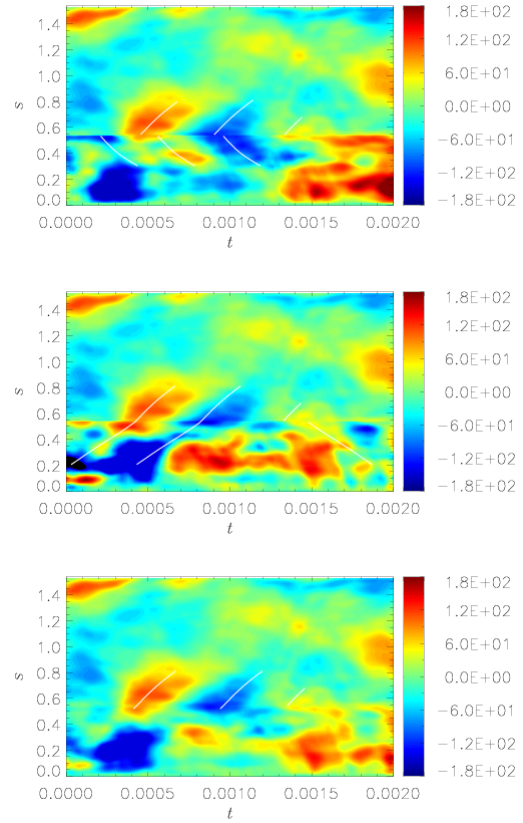


**Figure 9.** Azimuthal velocity,  $\langle \overline{u_\phi} \rangle'$ , for the run 6.5R5.

#### 4.4 Bandpass filtering

465

In order to observe TOs more clearly in our simulation data we perform bandpass filtering on our  $ts$ -data from section 4.2. Hence we perform a Fourier transform on the data in the  $t$ -direction and filter frequencies using a step function. This is a similar analysis to that performed by Gillet et al. (2010) albeit on our synthetic data rather than observational data.

Figs 12 to 15 show  $ts$ -data for several of our simulations that has been filtered of certain frequencies. The plots in each figure follow the same layout as previous figures so from top to bottom: data for ITCN, ITCS and the average over the entire  $z$ -average, respectively. In all of our runs we find that filtering out higher frequencies allows us to

478

better identify the TOs in our data. Fig. 12, for run 5R5, further highlights the two TOs that were identified in this data previously (cf. Fig. 7). This data has been filtered of frequency modes above 4 (as well as the mean). If we instead filter these low frequency modes out of the data we remove the structures travelling at the correct Alfvén speed. We can see this in Fig. 13, again for run 5R5, where all but frequency modes 6 to 8 are filtered. The structures present in  $\langle \overline{u_\phi} \rangle'$  no longer follow the trajectories given by the white curves and instead move outwards at a faster rate.

487

Further bandpass filtered plots for  $\langle \overline{u_\phi} \rangle'$ , also over the frequency modes 2 to 4, for runs 6.5R2 and 6.5R5 are presented in Figs 14 and 15, respectively. We have omitted plots

490



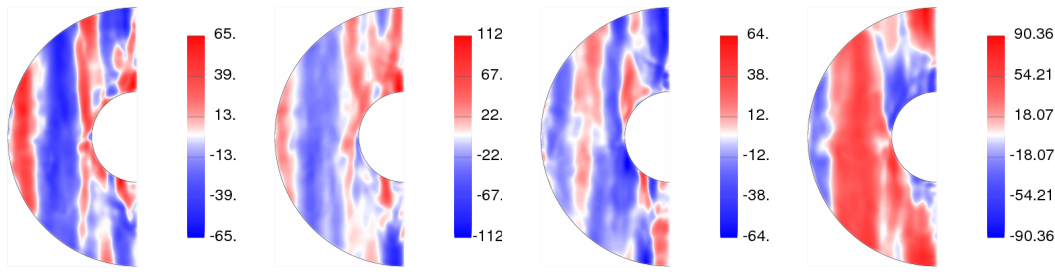


**Figure 11.** Series of snapshots of  $\overline{u_\phi'}$  for the run 4R5. Panels from left to right are at the following times:  $t = 0.009$ ,  $t = 0.010$ ,  $t = 0.012$ , and  $t = 0.014$ .

491 filtered of higher frequencies for runs 6.5R2 and 6.5R5 due to  
 492 their similarity to the plots of Fig. 13. All data filtered over  
 493 ranges other than approximately modes 2 to 4 only show  
 494 structures moving at rates inconsistent with the TO Alfvén  
 495 speed.

496 Fig. 14 allows us to identify a complicated structure of  
 497 inwards and outwards propagating waves OTC near to the  
 498 TC, which was not immediately obvious in the earlier un-  
 499 filtered plots (cf. Fig. 8). It is clear that some inwards  
 500 moving waves propagate through the TC and often into one hemi-  
 501 sphere only. For example the earliest instance of an inwards  
 502 propagating wave in Fig. 14 reaches the TC at  $t \simeq 0.0006$   
 503 and passes through into the region ITCS but not in the  
 504 northern hemisphere.

505 Filtering all but low frequency structures again high-  
 506 lights the previously identified TOs in Fig. 15, for run 6.5R5  
 507 (cf. Fig. 9). In fact, several of the features previously iden-  
 508 tified have only become clear upon filtering. We can clearly see  
 509 the structures propagating outwards from the TC, as well  
 510 as inwards from the TC in the northern hemisphere. Con-  
 511 versely, the structures ITC in the southern hemisphere propa-  
 512 gate outwards and through into the region OTC. This run,  
 513 in particular, highlights the complicated nature of waves inci-  
 514 dent on the TC.

515 The sensitivity in the bandpass filtering and preference  
 516 for low frequency modes draws our attention to two points.  
 517 Firstly, it validates our choice of  $\tau$  for each run since TOs  
 518 appearing at low frequencies implies that they do indeed op-  
 519 erate on the  $\tau$  timescale. Secondly, the lack of TOs appearing  
 520 at higher frequencies also suggests that TOs do not operate  
 521 on timescale much smaller than  $\tau$ . This was not immediately  
 522 obvious from our unfiltered data.

#### 523 4.5 Excitation mechanisms

524 We now explore the role various forces have in the driving of  
 525 the torsional waves observed in sections 4.2 and 4.4. In sec-  
 526 tion 3.1 we discussed how there were three possible driving  
 527 forces in our system and hence we plot quantities appearing  
 528 on the right-hand-side of (19). Since we aim to find correla-  
 529 tion between these forcing terms and the origins of TOs we  
 530 retain, on our plots throughout this section, the white curves  
 531 from the associated azimuthal velocity plots of sections 4.2  
 532 and 4.4. However, in our  $ts$ -contour plots for  $F_R$ ,  $F_V$  and  
 533  $F_{LD}$ , we do not expect features to be travelling along the

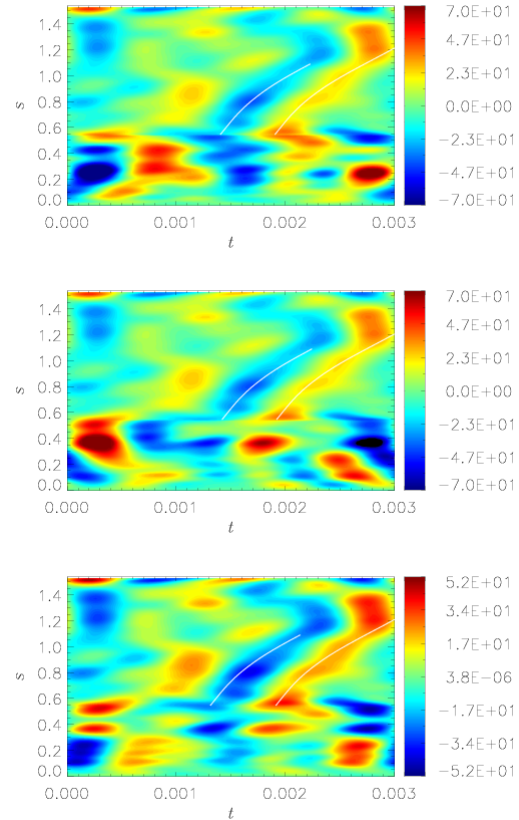


**Figure 12.**  $\langle \overline{u_\phi} \rangle$  bandpass filtered over modes 2 to 4, for the run 5R5.

534 white curves; rather we expect to find features at the origins  
 535 of the curves.

536 From Fig. 16, displaying forcing terms for run 5R5 (for  
 537 the regions OTC and ITCS only), we can make several obser-  
 538 vations. All three forces are weak for most of the region  
 539 OTC except at the TC itself. The viscous dissipation and  
 540 the Lorentz forcing are also strong at the equator, where the  
 541 rapid changes in velocity due to the CMB boundary layer  
 542 have a significant effect. Within the TC all three forces, but  
 543 especially  $F_V$  and  $F_{LD}$ , are larger. However, one of the most  
 544 striking features of these plots in the context of TO driving  
 545 is the excellent correlation between large Reynolds force at  
 546 the TC and the excitation of waves represented by the ori-

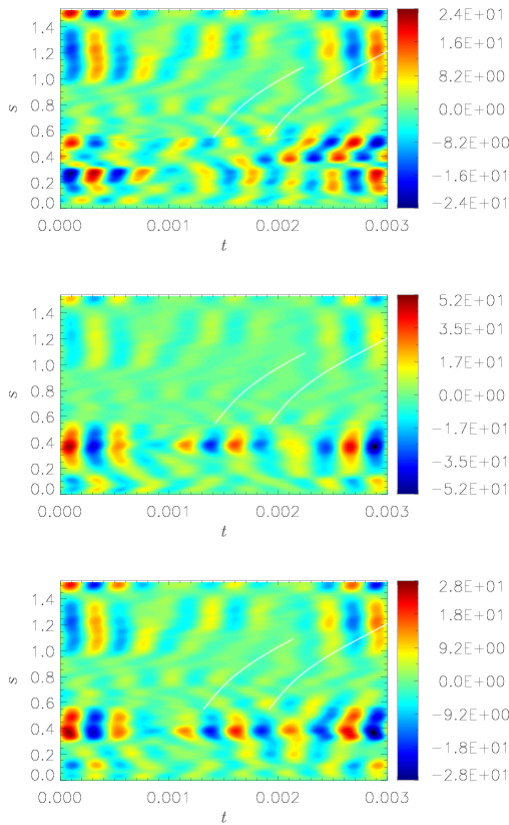


**Figure 13.**  $\langle \overline{u_\phi} \rangle$  bandpass filtered over modes 6 to 8, for the run 5R5.

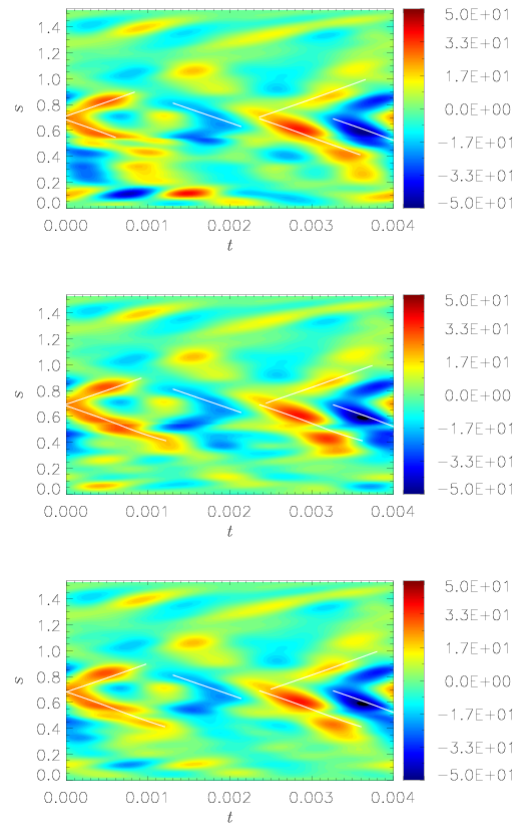


**Figure 14.**  $\langle \overline{u_\phi} \rangle$  bandpass filtered over modes 2 to 4, for the run 6.5R2.

gin of the two curves. Although the Reynolds force is clearly weaker than the Lorentz forcing (by approximately a factor of three), its correlation is superior since there are regions of large Lorentz force that do not coincide with TO initiation. Conversely, whenever the Reynolds force is large at the TC, a TO is produced.

In Fig. 17 we again plot forcing terms, this time for run 6.5R5. The plots for the three forces are broadly similar to the 5R5 case OTC. Once again the locations of the origin of identified TOs are well correlated with large regions of Reynolds force, this time ITC. A lack of correlation of large  $F_R$  at the TC with the waves propagating outwards there suggests that the waves ITC do indeed traverse the TC and thus do not require an excitation mechanism at the TC in this case. Evidence for correlation between Reynolds forcing and TO excitation comes not only from Figs 16 and 17, but from a series of snapshots from our runs, too numerous to display here.

## 5 DISCUSSION

Through our numerical simulations we have observed torsional oscillations at a range of Ekman numbers including at the relatively large  $E = 10^{-4}$ . These oscillations are able to propagate either inwards or outwards in the cylindrical radial direction. The torsional waves travel fastest under parameter regimes that promote the production of strong

magnetic fields. Thus, large magnetic Prandtl number and rapidly rotating regimes produce the quickest oscillations.

Torsional oscillations are often found to propagate from the TC, both inwards and outwards. Hence we have observed waves ITC, a region of the spherical shell not considered in previous work. Although waves are mostly found to originate at the TC, it is possible for excitation to occur at other locations in the shell. This indicates a complicated non-uniform excitation mechanism with various processes likely to excite oscillations at the different locations.

Within our set of simulations we identified two dynamo regimes for which a given system is able to organise itself. Whether the dynamo is in a weak or strong field regime has implications on the torsional waves observed. Weak field regimes found at  $Pm \in [1, 3]$  for a range of Ekman numbers are able to produce approximately equal numbers of inward and outward propagating waves. Conversely, strong field regimes found at  $Pm \in [3, 5]$  are dominated by waves of outwards propagation. Plots (and movies) of meridional sections of  $\overline{u_\phi}'$  are able to show the outwards propagation of columns in strong field runs whereas the same graphics show features more reminiscent of standing waves in the weak field runs. The speed of waves is found to best match that predicted for the Earth in the strong field regime with a core travel time of between 4 and 6 years.

Oscillations observed ITC almost exclusively originate at the TC and thus move radially inwards. This is either via an excitation mechanism at the TC or by a wave propagating

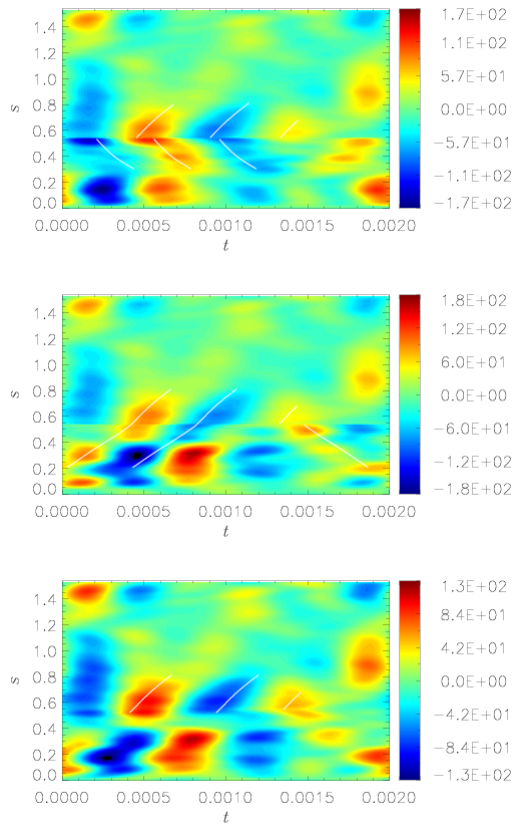


**Figure 15.**  $\langle \overline{u_\phi} \rangle$  bandpass filtered over modes 2 to 4, for the run 6.5R5.

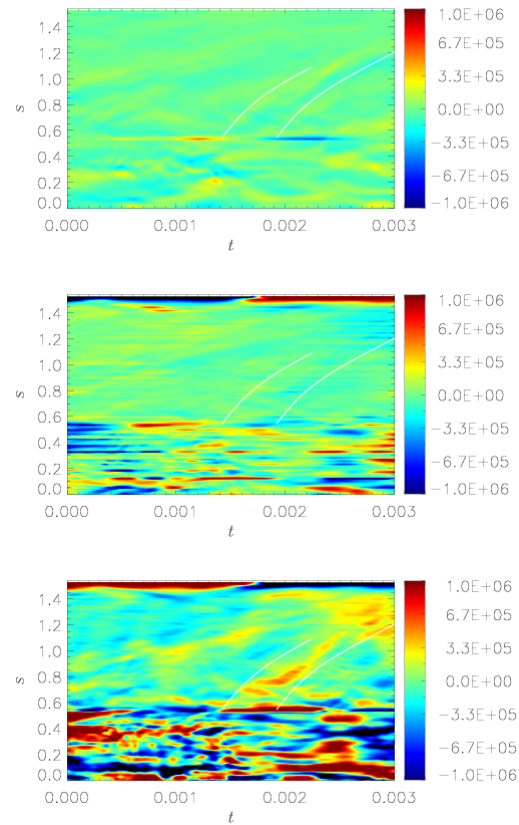


**Figure 16.** Forcing terms for ITCS and OTC for the run 5R5. From top to bottom:  $F_R$ ,  $F_V$  and  $F_{LD}$ .

600 across the TC from OTC. Additionally, weak field regimes  
 601 are more likely to promote torsional oscillations within the  
 602 TC. If waves are being excited at the TC then the weak field  
 603 regime, with its greater ability to promote inwards propaga-  
 604 tion, is naturally preferred for disturbances ITC. Conversely,  
 605 the preference for outwards movement in the strong field  
 606 regime leads to disturbances at the TC commonly travelling  
 607 through the region OTC towards the equator.

608 One of the most intriguing results from our simulations  
 609 is the apparent ability of waves to cross the tangent cylinder.  
 610 Waves can cross in either direction, however waves enter-  
 611 ing the region ITC often dissipate quickly, probably owing  
 612 to the large viscous dissipation there. Features propagating  
 613 from OTC are often absorbed into only one hemisphere ITC  
 614 suggesting that conditions and flow patterns have to be de-  
 615 sirable, in a given hemisphere, for a crossing of the TC to  
 616 take place in this direction. The crossing of waves in the  
 617 opposite direction is possible but rarer. The likelihood of  
 618 movement of oscillations into the region OTC is increased  
 619 if waves are found to be approaching the TC in each hemi-  
 620 sphere approximately concurrently. Since the regions north  
 621 and south of the inner core effectively act independently,  
 622 propagation from ITC to OTC is a random and often infre-  
 623 quent phenomenon resulting in the scarcity of such events.  
 624 One of our most studied simulations (6.5R5) was one of the  
 625 few to display propagation of waves from ITC to OTC.

626 We have been able to investigate the excitation mecha-  
 627 nisms of torsional waves within our simulations. We split

628 these into three categories, the damping due to viscous  
 629 forces, the Reynolds forces, and the Lorentz forces. We  
 630 have shown that the Lorentz force can be usefully divided  
 631 into that part which gives the restoring force of the tor-  
 632 sional oscillation itself, and the part that comes from the  
 633 ageostrophic convection. Although the convection is rela-  
 634 tively small-scale, the Lorentz force it produces does not  
 635 vanish when averaged over the Taylor cylinder, and may be  
 636 an important excitation mechanism for TOs.

637 Despite the Reynolds force consistently being the weak-  
 638 est of the three forces, correlation with TO propagation  
 639 from the TC leads us to conclude that it is also an im-  
 640 portant excitation mechanism in our simulations. At lower,  
 641 more Earth-like, Ekman numbers the Reynolds forcing will  
 642 inevitably become small relative to the Lorentz force and  
 643 may play a diminished role. However, the thin region near  
 644 the TC may well become thinner at low Ekman number,  
 645 so the velocity gradients driving the Reynolds force might  
 646 be sufficient to have an effect even though the velocity it-  
 647 self is small in magnitude. The scaling of the relative size of  
 648 the Reynolds and Lorentz contribution with Ekman num-  
 649 ber needs to be explored further, but this will require a new  
 650 approach, as reducing the Ekman number is notoriously ex-  
 651 pensive in full geodynamo simulations. The Lorentz force ex-  
 652 cited by ageostrophic convection, which seems particularly  
 653 strong inside the TC, is currently the preferred explanation  
 654 of TO excitation in the Earth's core.

655 Viscous forces were found to be significant near the



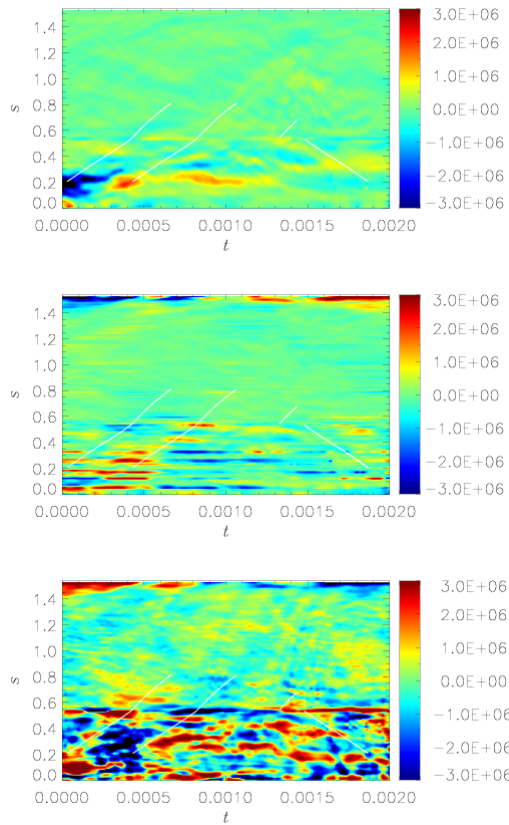


**Figure 17.** Forcing terms for ITCS and OTC for the run 6.5R5. From top to bottom:  $F_R$ ,  $F_V$  and  $F_{LD}$ .

CMB equator and inside the TC in our models, though we expect their impact to be much reduced at the very low Ekman numbers of the Earth's core. Their damping effect may be replaced by electromagnetic coupling with the mantle and the inner core, which has not yet been included in our model.

Several of the observations from our results highlight a common problem in numerical geodynamo simulations: we are restricted by limited computing resources when attempting to reach a parameter regime that can quantitatively replicate many of the geodynamo's features, including torsional oscillations. A reduction of geometric complexity by considering, for example, magnetoconvection in an annulus would help to alleviate this problem by allowing one to perform simulations at more realistic Ekman numbers. Alternatively, spherical geometry could be retained and a lower Ekman number achieved by performing simulations of magnetoconvection where the requirement of a long period of time integration to ensure a dynamo state is found is not necessary. These topics are the subject of future work.

## References

- Alfvén, H., 1942. Existence of electromagnetic-hydrodynamic waves, *Nature*, **150**, 405–406.
- Bloxham, J., Zatman, S., & Dumberry, M., 2002. The origin of geomagnetic jerks, *Nature*, **420**, 65–68.

- Braginsky, S., 1970. Torsional magnetohydrodynamic vibrations in the earth's core and variation in day length, *Geomag. Aeron.*, **10**, 1–8.
- Braginsky, S., 1984. Short-period geomagnetic secular variation, *Geophys. Astrophys. Fluid Dynam.*, **30**, 1–78.
- Buffett, B., Mound, J., & Jackson, A., 2009. Inversion of torsional oscillations for the structure and dynamics of Earth's core, *Geophys. J. Int.*, **177**, 878–890.
- Busse, F. & Simitev, R., 2005. Convection in rotating spherical fluid shells and its dynamo states, in *Mathematical aspects of natural dynamos*, pp. 359–392, eds Soward, A., Jones, C., Hughes, D., & Weiss, N., CRC Press.
- Christensen, U., Aubert, J., & Hulot, G., 2010. Conditions for earth-like geodynamo models, *Earth Planet. Sci. Lett.*, **296**, 487–496.
- Dormy, E., Soward, A., Jones, C., Jault, D., & Cardin, P., 2004. The onset of thermal convection in rotating spherical shells, *J. Fluid Mech.*, **501**, 43–70.
- Dumberry, M. & Bloxham, J., 2003. Torque balance, Taylor's constraint and torsional oscillations in a numerical model of the geodynamo, *Phys. Earth Planet. Inter.*, **140**, 29–51.
- Gillet, N., Jault, D., Canet, E., & Fournier, A., 2010. Fast torsional waves and strong magnetic field within the earth's core, *Nature*, **465**, 74–77.
- Gubbins, D. & Bloxham, J., 1985. Geomagnetic field analysis. part iii. magnetic fields on the core-mantle boundary, *Geophys. J. R. Astr. Soc.*, **80**, 695–713.
- Hori, K., Wicht, J., & Christensen, U., 2010. The effect of thermal boundary conditions on dynamos driven by internal heating, *Phys. Earth Planet. Int.*, **182**, 85–97.
- Jackson, A., 1997. Time dependence of geostrophic core-surface motions, *Phys. Earth Planet. Inter.*, **103**, 293–311.
- Jault, D., Gire, C., & LeMouél, J.-L., 1988. Westward drift, core motion and exchanges of angular momentum between core and mantle, *Nature*, **333**, 353–356.
- Jones, C., 2011. Planetary magnetic fields and fluid dynamos, *Ann. Rev. Fluid Mech.*, **43**, 583–614.
- Jones, C., Boronski, P., Brun, A., Glatzmaier, G., Gastine, T., Miesch, M., & Wicht, J., 2011. Anelastic convection-driven dynamo benchmarks, *Icarus*, **216**, 120–135.
- Roberts, P. & Aurnou, J., 2012. On the theory of core-mantle coupling, *Geophys. Astrophys. Fluid Dynam.*, **106**(2), 157–230.
- Sakuraba, A. & Roberts, P., 2009. Generation of a strong magnetic field using uniform heat flux at the surface of the core, *Nature Geosci.*, **2**, 802–805.
- Schaeffer, N., Jault, D., Cardin, P., & Drouard, M., 2012. On the reflection of Alfvén waves and its implication for Earth's core modelling, *Geophys. J. Int.*, **191**, 508–516.
- Taylor, J., 1963. The magneto-hydrodynamics of a rotating fluid and the earth's dynamo problem, *Proc. Roy. Soc. A*, **274**, 274–283.
- Wicht, J. & Christensen, U., 2010. Torsional oscillations in dynamo simulations, *Geophys. J. Int.*, **181**, 1367–1380.
- Zatman, S. & Bloxham, J., 1997. Torsional oscillations and the magnetic field with the earth's core, *Nature*, **388**, 760–761.